FLOW **CAMBRIDGE**
UNIVERSITY PRESS

RESEARCH ARTICLE

Inferring free surface disturbance properties from Kelvin wakes using convolutional neural network

Xuanting Hao (iD)

Department of Mechanical and Aerospace Engineering and Scripps Institution of Oceanography, University of California San Diego, La Jolla, CA, USA
Corresponding author: x3hao@ucsd.edu

Abstract

Kelvin wakes are fluid motions generated by a moving disturbance at a free surface. We present a machine learning-based framework for inferring the properties of such moving disturbances from the Kelvin-wake patterns. We perform phase-resolved simulations to establish a dataset of nearly half a million Kelvin wakes generated by disturbances of varying propagating speed, length scale and geometry. Trained with the augmented data, the neural network achieves accuracies of 99.7% and 92.4% in predicting the velocity and the length scale of the disturbance, respectively, even if a random noise has been added to the training data. The explainability of the neural network is demonstrated by quantifying the contribution of the input data to the prediction, which shows a strong connection with the diverging and transverse waves. The accuracy of the neural network in predicting the disturbance length scale is sensitive to wave nonlinearity.

Impact Statement

Ship wakes are known to influence coastal sediment transport and affect the habitats of marine life. Monitoring ships is crucial for enforcing drug and fishery regulations as well as for controlling port traffic. In this study, we apply a machine learning-based technique to analyse surface disturbances that can serve as indicators of real ships. Our findings demonstrate the effectiveness of convolutional neural networks in characterising both the velocity and length scale of ships from their wakes. Consequently, this technique has the potential to greatly enhance ship monitoring in operational settings.

---

1. Introduction

A distinct wave pattern is generated when a disturbance moves at a constant speed at the water's surface. This phenomenon, also known as the Kelvin wake (Thomson, 1887), has been extensively studied because the wake structure is closely related to the kinematics and geometry of the sources of the disturbance. Note that Kelvin wakes should not be mistaken for Kelvin waves, which are produced by the geostrophic balance between the Coriolis force and gravity in the direction transverse to wave propagation (Kundu *et al.,* 2016). Ship-induced Kelvin wakes represent an important anthropogenic impact in the coastal environment. For instance, a recent study measured the shipping events in the Venice Lagoon and identified ship wakes as one of the causes of shoreline erosion (Scarpa *et al.,* 2019). Hence,

understanding the hydrodynamics of these ship-related motions is critical for reducing their adverse environmental impact. On the other hand, ship wakes have enabled the remote sensing-based monitoring of maritime traffic, in which the ship's location and velocity data prove valuable for ship collision prevention.

Because of the complexity in surface wave–ship structure interaction, the study of Kelvin wakes is often facilitated by applying a moving pressure to the free surface of an ideal fluid. For selected disturbance velocity and geometry, one can then derive an analytical solution for the wake angle, φ_{max}, defined as the angle between trendlines consisting of local maxima of the surface elevation. In linear theory (Thomson, 1887), φ_{max} was found to be a constant value of arcsin$(1/3) = 19.5°$, independent of the speed of the disturbance. However, this was found to contradict observations. Rabaud and Moisy (2013) examined satellite images of ship wakes and obtained a scaling law for large Froude numbers $\varphi_{max} \sim Fr^{-1}$ by arguing that the waves generated by the surface disturbance may not exceed the ship length L, which imposes a lower limit on the characteristic wavenumber of the wake (here, $Fr = U/\sqrt{gL}$, where U is the ship velocity and g is the acceleration due to gravity). This hypothesis was later proved unnecessary as Darmon *et al.* (2014) derived the asymptotic value of the angle corresponding to the maximum amplitude of the waves and reproduced the same scaling law. In a following study, Benzaquen *et al.* (2014) extended their result to an elliptical pressure disturbance and discovered the relation $\varphi_{max} \sim \sqrt{W}/Fr$, where W is the ellipse aspect ratio. Miao and Liu (2015) studied the wave patterns formed when the pressure disturbance is arbitrary. By decomposing the pressure into Fourier components and integrating the surface response corresponding to each individual component, they found that φ_{max} may be a complex function of the Froude number. For example, they showed that, in the presence of a rectangular uniform pressure, the scaling law becomes $\varphi_{max} \sim Fr^{-2}$. It is worth noting that φ_{max} is a nonlinear function of the disturbance parameter (e.g. the speed U), even for an infinitesimally small pressure disturbance, and the resulting linear wave response (see the scaling laws mentioned above). Besides the aforementioned transition with Froude number, the wake angle is also known to be a function of the disturbance geometry. In general, a theoretical expression derived from asymptotic analysis is applicable only to highly idealised free surface disturbances.

Ship detection and characterisation from remote sensing images is an active area of research, where the objectives may include identification of a ship and the prediction of the ship's velocity. A widely used technique for wake identification is the Radon transform (e.g. Copeland *et al.,* 1995), which integrates a raw two-dimensional (2-D) signal along all possible lines. Hence, the Radon transform performs best when used for identifying linear patterns in an image, such as the asymptotic wakes mentioned above. However, the wake angle is not a well-defined variable, as the definition of a local maximum of the surface elevation can be ambiguous as a result of the contamination by background surface waves and the observational errors in remote sensing. Recent years have seen the application of emerging machine learning techniques to the inverse problems in ship wake characterisation. For example, dynamic mode decomposition, an unsupervised learning technique, has been applied to the separation of the ship wake pattern from the background wind waves (Zhang and Jiang, 2020). Supervised learning methods based on the convolutional neural network (CNN) have also been used for detecting ship wakes from remote sensing images. Kang and Kim (2019) applied CNN to satellite images, where the output data of the neural network are the latitude and longitude coordinates of a subregion marked as the ship, wake or sea. The ship velocity was then estimated from the azimuth offset by performing edge detection and Radon transform of the subregion. In another study (Xue *et al.,* 2022), the output of the CNN not only includes the coordinates of a subregion, but also the ship's location and the angle of the wakes. A majority of these studies focus on the feasibility and accuracy in terms of operational applications while neglecting the hydrodynamics constraints.

In this study, we investigate the inverse problem of inferring the properties of a moving disturbance from Kelvin wakes using CNNs. Unlike existing studies that typically focus solely on predicting velocity, we explore the potential of CNNs to simultaneously predict both velocity and the disturbance length scale. Additionally, we aim to interpret the CNN's prediction capabilities and assess the impact of wave

nonlinearity on accuracy. The remainder of this paper is organised as follows. In § 2, we introduce the techniques needed for building the prediction framework, which include a phase-resolved wave model for obtaining the training and testing data, the mathematical function for a free disturbance and the neural networks used. We outline the simulation set-up and training data generation in § 3. The training results are provided in § 4. Conclusions are given in § 5.

2. Methodology

2.1 Wave model

In this study, we assume that the water is incompressible, inviscid and irrotational, while the ship is modelled as a surface pressure disturbance. This strategy allows for an acceptable computational cost and has been widely used in theoretical and numerical studies of Kelvin wakes (see e.g. Benzaquen *et al.,* 2014; Miao and Liu, 2015; Pethiyagoda *et al.,* 2021). In the present study, the deep-water assumption is adopted, as the focus is on the generation of Kelvin wakes. In future studies, their impact on sediment transport can be evaluated as these waves propagate into shallower waters. Under the potential flow assumption, it can be shown that the surface gravity waves in deep water are uniquely determined by the surface elevation $\eta(x, y, t)$ and the surface velocity potential $\Phi^S(x, y, t) \equiv \Phi(x, y, \eta(x, y, t), t)$ (Zakharov, 1968).

For a steady pressure distribution moving at a constant speed U, it is convenient to rewrite the Zakharov equations in the moving frame of reference (Dommermuth and Yue, 1988)

$$\eta_t - U\eta_x + \nabla\eta \cdot \nabla\Phi^S - (1 + \nabla\eta \cdot \nabla\eta)W_S = 0, \tag{2.1}$$

$$\Phi_t^S - U\Phi_x^S + g\eta + \frac{1}{2}\nabla\Phi^S \cdot \nabla\Phi^S - \frac{1}{2}(1 + \nabla\eta \cdot \nabla\eta)W_S^2 + \frac{p_a(\boldsymbol{x})}{\rho_w} = 0, \tag{2.2}$$

where the gradient operator in the horizontal plane is defined as $\nabla \equiv (\partial/\partial x, \partial/\partial y)$, $\boldsymbol{x} = (x, y)$ is the horizontal coordinate vector, $W_S = \Phi_z$ is the surface vertical velocity, $p_a(\boldsymbol{x}, t)$ is the external pressure disturbance imposed at the surface and ρ_w is the density of water.

The above equations can be solved with the high-order spectral (HOS) method (Alam *et al.,* 2009; Alam, 2012; Dommermuth and Yue, 1987) in a periodic domain by assuming that the velocity potential can be expanded in a perturbation series $\Phi(\boldsymbol{x}, z, t) = \sum_1^M \Phi^{(m)}(\boldsymbol{x}, z, t)$ with respect to a characteristic wave steepness, where M is the maximum perturbation order. At each order, it is assumed that $\Phi^{(m)}$, as Φ, satisfies the Laplace equation, $\nabla^2\Phi^{(m)} = 0$, and the deep-water boundary condition, $\nabla\Phi^{(m)}(\boldsymbol{x}, z \to -\infty, t) \to 0$. Further assuming periodic boundary conditions in the horizontal directions, $\Phi^{(m)}$ can be written as the eigenfunction of the Laplace equation

$$\Phi^{(m)}(\boldsymbol{x}, z, t) = \sum_{j=1}^{\infty}\sum_{l=1}^{\infty} \Phi_{jl}^{(m)}(t) \exp\left(|\boldsymbol{k_{jl}}|z + i\boldsymbol{k_{jl}} \cdot \boldsymbol{x}\right), \tag{2.3}$$

where $\Phi_{jl}^{(m)}(t)$ are the Fourier coefficients to be calculated from $\Phi^{(S)}$, and $\boldsymbol{k_{jl}} = (2j\pi/L_x, 2l\pi/L_y)$, with L_x and L_y being the computational domain size in the x and y directions, respectively. To determine $\Phi_{jl}^{(m)}(t)$, the Dirichlet problem is first solved

$$\begin{cases} \psi^{(1)} = \Phi^S(x, y, t), \quad m = 1 \\ \psi^{(m)} = -\sum_{l=1}^{m-1} \dfrac{\eta^l}{l!}\dfrac{\partial^l\psi^{(m-l)}}{\partial z^l}. \quad m = 2, 3, \cdots, M, \end{cases} \tag{2.4}$$

where $\psi^{(m)} \equiv \Phi^{(m)}(\boldsymbol{x}, 0, t)$, $m = 1, 2, \cdots, M$. Subsequently, the coefficients $\Phi_{jl}^{(m)}(t)$ can be computed in an efficient manner by taking the 2-D Fourier transform of $\psi^{(m)}$.
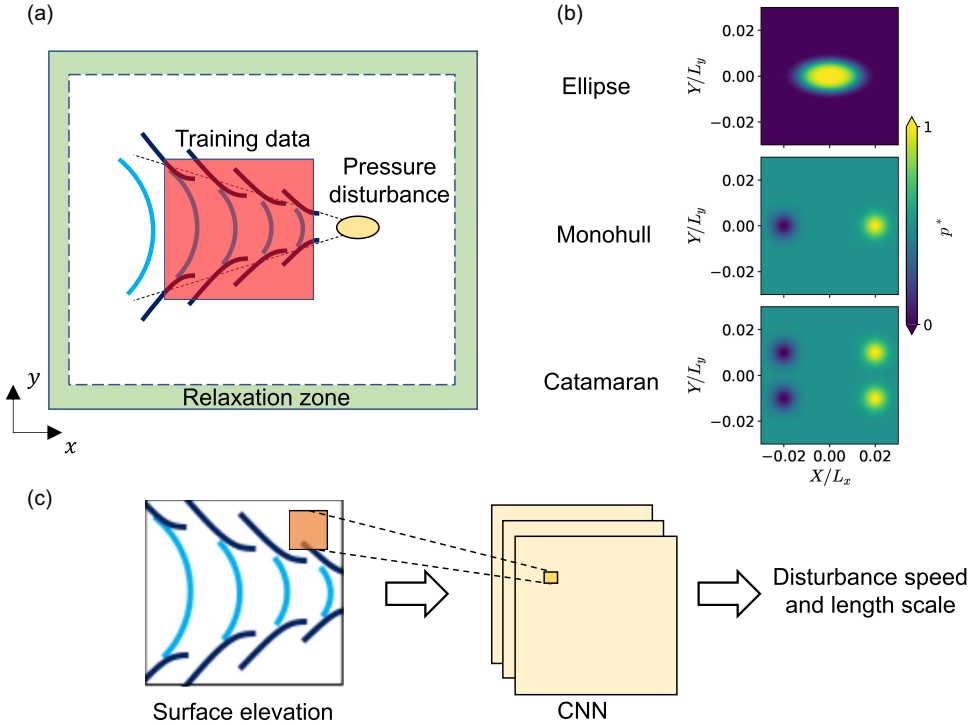
Figure 1. *Schematic of (a) the computational domain, (b) the pressure distributions representing different ship types and (c) the CNN-based prediction framework. In (a), the region for extracting the training data is marked by the shaded square in red. In (b), the coordinates are shifted such that the geometric centres of the pressure distributions are at the origin (i.e. $X = x - x_c$ and $Y = y - y_c$), and the normalised pressure is defined as $p* = (p - p_{min})/(p_{max} - p_{min})$, where p_{min} and p_{max} denote the minimum and maximum pressures.*

The vertical velocity at the free surface is calculated by

$$W_S = \sum_{m=1}^{M} \sum_{l=0}^{M-m} \frac{\eta^l}{l!} \frac{\partial^{l+1} \psi^{(m)}}{\partial z^{l+1}}. \tag{2.5}$$

The system can then be integrated in time from η and Φ^S prescribed at $t = 0$. While the HOS method was originally developed for solving the Zakharov equations, it can also be directly applied to the system in the moving frame of reference (Dommermuth and Yue, 1988; Miao and Liu, 2015). To avoid numerical instabilities caused by excessive local steepness, an adaptive low-pass filter may be applied to η and Φ^S at each time step when $M > 1$ (Xiao *et al.*, 2013).

2.2 Pressure disturbance

In our simulations, the pressure disturbance is placed near the end of the domain to allow for the wake pattern formation (see figure 1a). To reduce wave reflection, we impose a relaxation zone at the boundaries of the computational domain (Mei et al., 2005). In the present study, we consider three types of pressure distributions that have been widely used in previous studies for generating Kelvin wakes. For each type of pressure distribution, an example of their spatial distribution is shown in figure 1(b).

For an elliptical pressure distribution, we follow the definition of Dommermuth and Yue (1988)

$$P_e(x, y) = P_0 e^{-\Pi(r/R)}, \tag{2.6}$$

where $r = (X^2 + Y^2/W^2)^{1/2}$, $X = x - x_c$, $Y = y - y_c$, P_0 is the peak magnitude of the pressure and Π is a smooth function. Here, x_c and y_c are the coordinates of the geometric centre, R is the radius of the ellipse and W is the ellipse aspect ratio. While the exact form of P_e varies slightly in different studies, the impact on the far-field Kelvin-wake pattern is expected to be small.

The pressure distribution corresponding to a monohull is defined as the sum of two circular distributions

$$P_m(x, y) = P_0 \left[e^{-\gamma\left[(X - L_h/2)^2 + Y^2\right]} - e^{-\gamma\left[(X + L_h/2)^2 + Y^2\right]} \right], \tag{2.7}$$

where L_h is the hull length and γ is the bow and stern geometry parameter.

The catamaran is defined as the sum of two monohull distributions at a distance of B

$$P_c(x, y) = P_m(x, y - B/2) + P_m(x, y + B/2). \tag{2.8}$$

2.3 Convolutional neural network

The basis of a CNN is the convolutional layer, which can be written as

$$\boldsymbol{B}_{i,j} = \sum_{l=-\Delta}^{\Delta} \sum_{m=-\Delta}^{\Delta} A_{l,m} \boldsymbol{w}_{i+l, j+m} + \boldsymbol{u}, \tag{2.9}$$

where A and B denote the input and output data of the layer, respectively, $\boldsymbol{w}$ is a weighting matrix, $\boldsymbol{u}$ is an optional bias matrix and Δ is the filter size. Both $\boldsymbol{w}$ and $\boldsymbol{u}$ are determined in the training process. Hence, $\boldsymbol{B}$ can be seen as the discretised convolution (more accurately, cross-correlation) between a 2-D array A and $\boldsymbol{w}$ when $\boldsymbol{u} = 0$. Hence, compared with a fully connected layer used in a multi-layer perceptron, a convolutional layer can identify the spatial structures of the data and is therefore suitable for image-like input.

LeNet-5 is a classical CNN architecture originally designed for handwritten digit recognition (Lecun *et al.,* 1998). It comprises three convolutional layers followed by pooling layers and two fully connected layers, which proved to be sufficiently accurate in classifying handwritten digits. While LeNet-5 demonstrated the power of CNNs in extracting spatial structures from 2-D data, it has a modest complexity compared with contemporary models. A more widely used modern CNN is the residual network (ResNet) (He *et al.,* 2016), which utilises the residual connections and addresses the vanishing gradient problem during training. The residual blocks enable the network to focus on the difference between the input and output of each layer, which significantly improves the network's ability to learn deeper representations and enhances its overall performance. In the present study, LeNet-5 and ResNet-18, a residual neural network with 18 layers, are used. The prediction framework is shown in figure 1(c) (see the Supplementary Material for the architectures of the CNNs).

2.4 Wave model validation

To demonstrate the accuracy and numerical capability of the HOS method, we perform simulations of Kelvin wakes produced by an elliptical pressure forcing applied to the free surface. We first vary the speed U (equivalently Fr) of the disturbance, while keeping the magnitude of the ellipse aspect ratio W and the semi-minor axis R constant (see dataset V_{Fr} in table 1). For the dataset V_{W}, we change the values of W instead. Figure 2(a) shows an example of the Kelvin wakes generated. Here, the normalised surface elevation is defined as $\eta^* = (\eta - \eta_{min})/(\eta_{max} - \eta_{min})$, where η_{min} and η_{max} denote the minimum and maximum elevations, respectively. From the instantaneous surface wave field, we identify the maximum elevation along each y direction and perform a linear regression to obtain the wake lines (see also the white dashed lines in figure 2a) and the wake angle φ_{max}. The Froude number is defined as $Fr = U/\sqrt{gR}$. The computed wake angles are then plotted as a function of Fr (figure 2b) and W (figure 2c), respectively. For both datasets, our simulation results agree well with the theoretical scaling law of $\varphi_{max} \sim \sqrt{W}/Fr$, derived by Benzaquen *et al.* (2014).

Table 1. *Parameters used in the HOS-based simulations for asymptotic analysis and model validation, where N_x and N_y are the grid numbers in the x and y directions, respectively, L is a characteristic length scale and U is the speed of pressure disturbance*

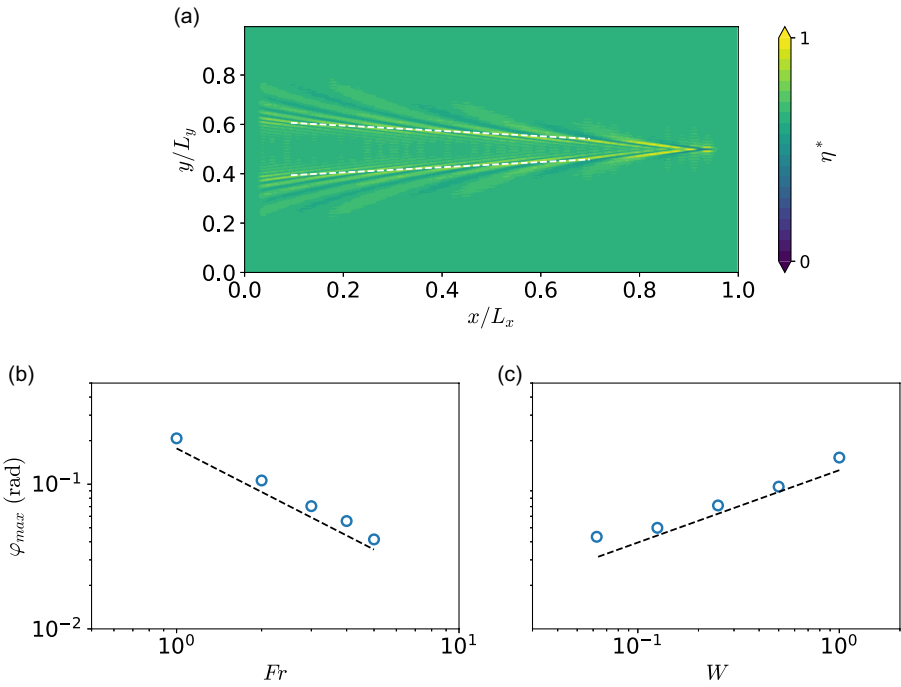| Datasets	M	N_x, N_y	$L_x/L, L_y/L$	$U/\sqrt{gL}$	R/L	W
V_{Fr}	1	256	200	$1.4 - 7.1$	2	0.5
V_W	1	512	400	8.9	20	$0.0625 - 1$
V_M	$2 - 5$	512	400	8.9	2	0.5

Figure 2. *Simulation results for validating the response of the wave system: (a) an example of the (normalised) surface elevation; (b) the maximum surface elevation angle as a function of Froude number; (c) the maximum surface elevation angle as a function of the ellipse aspect ratio. In (a), the locations of the local maximum surface elevation are denoted by the white dashed lines. The theoretical scaling law $\varphi_{max} \sim \sqrt{W}/Fr$ (Benzaquen et al., 2014) is denoted by the black dashed lines in (b) and (c).*

We then examine the nonlinear error related to the perturbation expansion in the HOS method. Let $\epsilon = \max(\eta_x^2 + \eta_y^2)^{1/2}$ denote the characteristic steepness of the surface wave field, the error $e = \|\eta_M - \eta_{true}\|$ then should scale as $e^{\sim} \epsilon_{(M+1)}$, where η_M is the surface elevation obtained from HOS simulations performed at order M and η_{true} is the corresponding ground truth. This strategy is equivalent to the validation of the HOS method by examining the error in Φ_z, which was adopted in the simulations of Stokes wave (Dommermuth and Yue, 1987) and nonlinear surface capillary waves (Pan, 2020). Ideally, η_{true} needs to be calculated from analytical solutions, such as the Crapper wave used by Pan (2020). However, no such solutions exist for the nonlinear waves generated by the moving pressure of an arbitrary shape and we treat $\eta_M(M = 5)$ as η_{true} instead.

Simulations are performed for $M = 2, 3, 4, 5$ (see datasets V_M in table 1). For each M, we repeat the simulations at different characteristic wave steepnesses by adjusting the strength of the peak pressure P_0. Figure 3 shows the variations of the normalised error e/e_0 with the steepness at different maximum

Table 2. *Parameters used in the HOS-based simulations for training data generation. Note that each case includes multiple simulation runs at varying parameters, and the subscripts 'e', 'm' and 'c' in the case names denote the ellipse, monohull and catamaran types of disturbance, respectively*

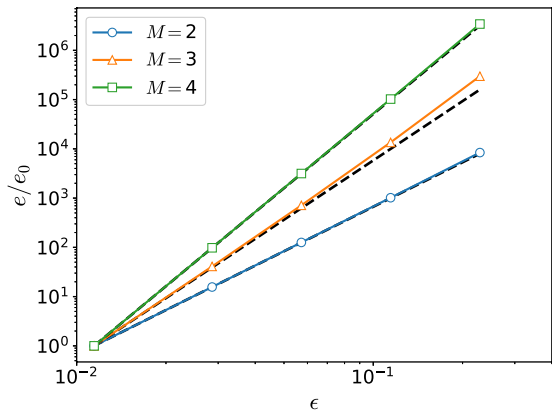| Datasets	N_x, N_y	$L_x/L, L_y/L$	$U/\sqrt{gL}$	R/L	W	$\gamma L_h{}^2$	L_h/L	B/L_h
T_e	1024	200	$0.6 - 3$	$2 - 5$	$0.125 - 1$	$-$	$-$	
T_m	1024	200	$0.6 - 3$	$-$	$-$	$1 - 400$	$1 - 10$	$-$
T_c	1024	200	$0.6 - 3$	$-$	$-$	$4 - 256$	$2 - 8$	$0.25 - 4$

Figure 3. *Simulation error as a function of the characteristic wave steepness. The errors are normalised by e_0, their corresponding values at the smallest steepness. The black-dashed lines correspond to the theoretical scaling of the error with the steepness $e \sim \epsilon^{M+1}$, where M is the maximum perturbation order used in the simulations.*

perturbation orders. As expected, the error growth with increasing M agrees well with the theoretical prediction.

3. Training data generation

We perform 787 simulations to generate the training data across a wide range of parameters (see datasets T_e, T_m and T_c in table 2). Since the length scales of the far-field Kelvin-wake patterns are often much larger than the characteristic size of the pressure distribution (see the validation cases in figure 2 for example), we choose larger grid numbers and smaller domain lengths compared with the validation cases to further reduce the impact of the (possible) Gibbs phenomenon. In all simulations, the surface elevation data are collected at a time instant when the Kelvin wakes are sufficiently close to the end of the domain. To reduce the computational cost, we set the pressure to an infinitesimally small amplitude and perform the simulations using the linear model by setting $M = 1$. We note that a novel machine learning-based technique has been developed to extend the HOS method, enabling predictions for ocean surface gravity waves to be made more than two orders of magnitude faster than with the original method (Mohaghegh *et al.*, 2021). This strategy offers an efficient way to generate data for future studies.

To obtain the input to the neural network, the far-field wake pattern η in the region of $(L_x/4 \le x \le 3L_x/4, L_y/4 \le y \le 3L_y/4)$ is first extracted from the raw simulation data such that the neural network does not memorise the surface pattern near the location of the pressure forcing (see figure 1a). A downsampling operation is then applied to the resulting 513×513 matrix to create the training data. Two spatial resolutions are considered: $(L_x/64, L_y/64)$ and $(L_x/128, L_y/128)$. The corresponding matrix sizes of the training data are 33×33 and 65×65, respectively. To increase the size of training samples, we then apply an affine transformation to the surface elevation data, including rotating between $0°$ and $360°$ at an interval of $10°$ and scale up to 160% of the original image. The details on data augmentation
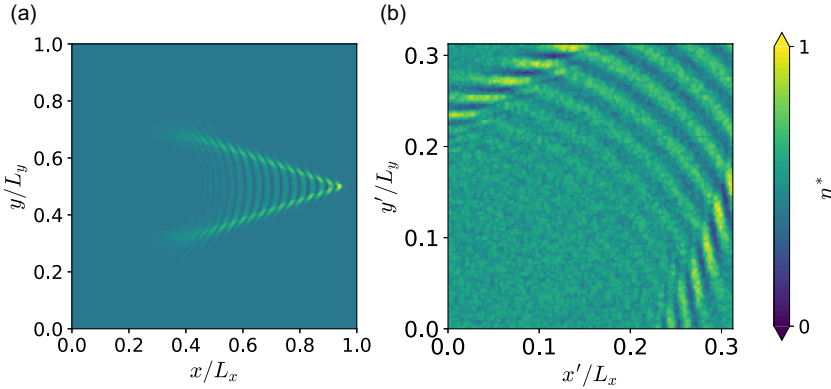
Figure 4. *An example of normalised surface elevation (a) computed using the HOS method (i.e. raw data); and (b) obtained from the raw data using augmentation technique.*

are provided in the Supplementary Material. To improve the training stability, the augmented surface elevation is normalised, $\eta* = (\eta - \eta_{min})/(\eta_{max} - \eta_{min})$. In the final step, different levels of random error up to 30 % of the maximum wave elevation are added to $\eta*$ to address the overfitting issue commonly faced in deep learning, resulting in 4.53×10^5 images in total as the input data (training data available in UC San Diego's data archive https://doi.org/10.6075/J0GH9JCX).

To demonstrate the effect of affine transformation, we show an example of the raw surface elevation data obtained from the HOS simulation (figure 4a) and the transformed data (figure 4b), obtained by performing a 50° rotation, scaling at a ratio of 1.6 uniformly in both directions, and adding a random noise of up to 30 % of $(\eta_{max} - \eta_{min})$. The output of the neural network includes the speed U and the length scale of the moving pressure L, which corresponds to R for the elliptical pressure distributions, and L_h for the monohull and catamaran distributions. A similar normalisation is performed to obtain the actual output of the neural network $\boldsymbol{v} = [U^* \, L^*]^T$ where $U^* = (U - U_{min})/(U_{max} - U_{min})$ and $L^* = (L - L_{min})/(L_{max} - L_{min})$.

In the training process, we define the loss function as the mean squared error between the neural network prediction and the ground truth $J = (\boldsymbol{v}_{pred} - \boldsymbol{v}_{true})^2$, where $\boldsymbol{v}_{pred}$ and $\boldsymbol{v}_{true}$ correspond to the CNN prediction and the ground truth of the vector $\boldsymbol{v} = [U^* \, L^*]^T$, respectively. The Adam optimiser is adopted and the initial learning rate is 0.001 (Kingma and Ba, 2015). All input images are first randomly shuffled and approximately 4.1×10^5 samples are then selected for training, while the other 4.5×10^4 samples are reserved for validation. Both models are used for training, and for the 65×65 input resolution, ResNet-18 has approximately 11 million parameters while LeNet-5 has 0.33 million.

4. Training results

4.1 Loss function and accuracy

For both models and input resolutions, the loss function converges within approximately 400 epochs (figure 5). At both resolutions, the LeNet-5 model shows a faster convergence rate than the ResNet-18 model because of its smaller parameter size. Meanwhile, the loss function decreases by approximately three orders of magnitude for the ResNet-18 model, which is significantly better than LeNet-5. We remark that using images at a different resolution may affect the performance of the ResNet-18 model.

To examine the performance of each model, we reconstruct the output vector $\boldsymbol{v}$ when the input data are selected from the validation data. The CNN predictions are plotted against the ground truth in figure 6 for resolution 65×65. For the velocity, the neural network shows an excellent performance with few outliers, whereas for the length scale, more outliers exist across all ranges of the length scale. We further define the accuracy function $A(x)$ as the percentage of validation data that satisfies $\|x_{pred} - x_{true}\|_2/\|x_{true}\|_2 < 5\%$, and evaluate its value for U and L, respectively. As shown in table 3,
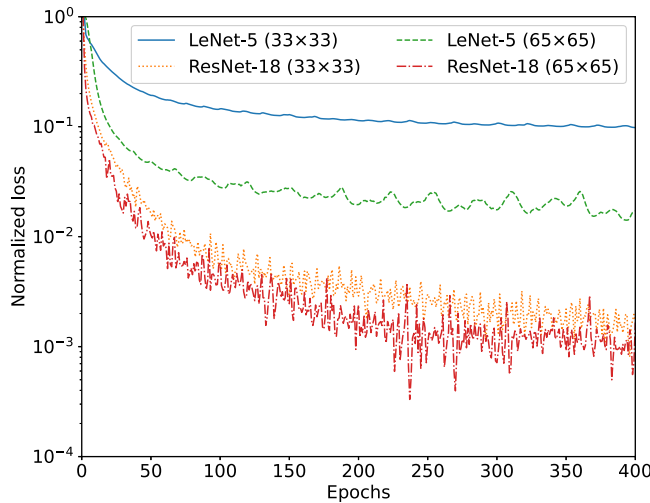
Figure 5. *Convergence of the loss function J normalised by its initial value J_0.*
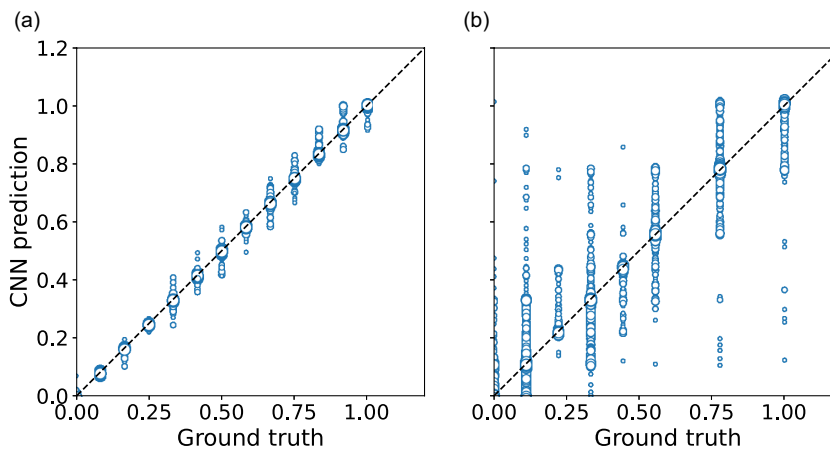

Figure 6. *The CNN prediction and ground truth of the normalised (a) velocity U^* and (b) length scale L^* of the disturbance. Plotted are results for ResNet-18 trained using images with a resolution of 65×65. The black dashed lines correspond to a perfect prediction. Here, the size of the markers increases with the number of data points they denote.*

increasing the input resolution from 33×33 to 65×65 appears to have limited impact on the prediction accuracy, while using the ResNet-18 model significantly increases the prediction performance. When ResNet-18 is used, the accuracy for predicting U is close to perfect. Despite the outliers observed in figure 6(b), the corresponding accuracy $A(L)$ is 92.4 %, suggesting that the ResNet-18 model can provide a reasonable prediction of the length scale. We have also examined the performance of ResNet-18 on local data, which generally shows a robust performance (see details in the Supplementary Material).

For comparison, an analysis based on the Radon transform (Radon, 1986) is performed for three selected examples of pressure disturbances (figure 7). These three examples are chosen such that the rotation angles used in the affine transformation for producing the training data are identical. Note that, for monohull and catamaran types of pressure disturbance, the wakes produced often show an interference

Table 3. *Summary of training configuration, loss and accuracy. Here, the normalised loss at convergence is calculated by taking the average of their values in the last 100 epochs*

CNN model	Input resolution	Loss at convergence J/J_0	$A(U)$	$A(L)$
LeNet-5	33×33	0.10	65.8%	15.3%
ResNet-18	33×33	1.8×10^{-3}	97.4%	77.4%
LeNet-5	65×65	1.9×10^{-2}	76.8%	19.4%
ResNet-18	65×65	1.2×10^{-3}	99.7%	92.4%
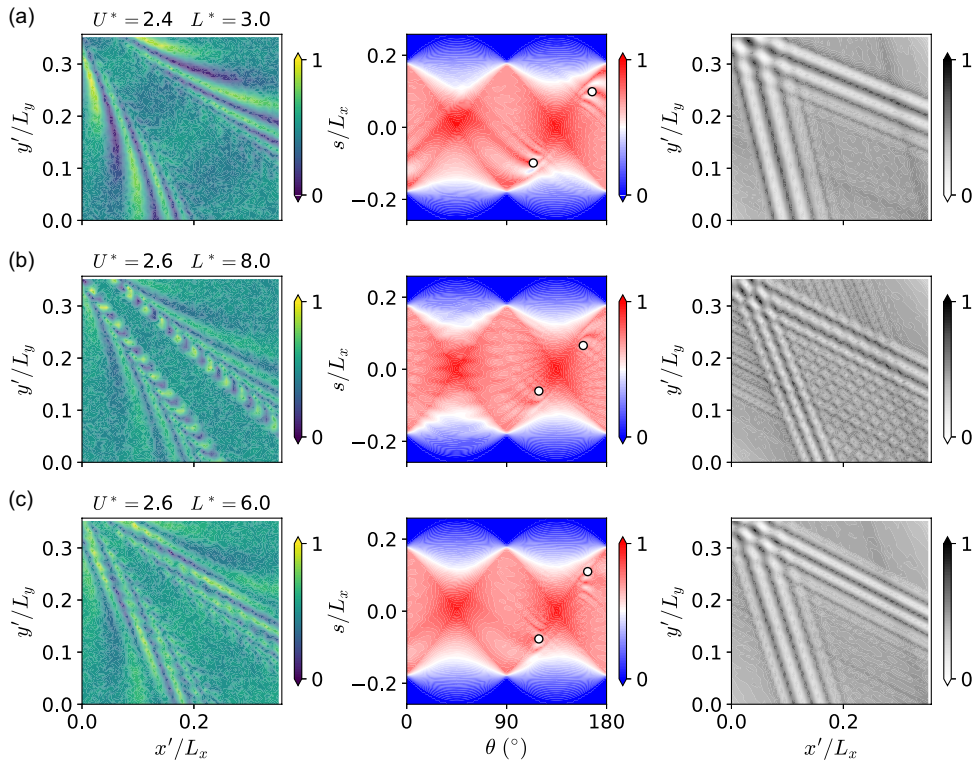
Figure 7. *Radon transform analysis for selected examples of pressure disturbances of type: (a) ellipse, (b) monohull and (c) catamaran. The left, middle and right columns correspond to the input data (i.e. the normalised surface elevation η^*), the Radon space of the data, $\mathbf{R}[\eta](\theta, s)$ and the reconstructed Kelvin wakes, $\hat{\eta}$, respectively. The reconstruction, $\hat{\eta}$, is computed using $\mathbf{R}[\eta](\theta_1, s)$ and $\mathbf{R}[\eta](\theta_2, s)$, where θ_1 and θ_2 correspond to the two local peaks (denoted by the white dots) in the Radon space.*

pattern (for more details, see the visualisations of the raw surface elevation at https://doi.org/10.6075/J0RN386Z). The mathematical expression for the Radon transform is given by

$$\mathbf{R}[\eta](\theta, s) = \int_{-\infty}^{\infty} \eta(z \sin \theta + s \cos \theta, -z \cos \theta + s \sin \theta)\mathrm{d}z, \qquad (4.1)$$

where θ is the angle of the line pattern, and s is the arc length. In practice, the integration limits should be replaced by the size of an image. Similar to the study by Zilman *et al.* (2004), the local peaks at angles θ_1 and θ_2 corresponding to the diverging wake patterns are identified (see the white dots plotted on $\mathbf{R}[\eta]$ in figure 7). Additionally, the surface elevation reconstructed from $\mathbf{R}[\eta](\theta_1, s)$ and $\mathbf{R}[\eta](\theta_2, s)$ reproduces the line patterns of the asymptotic wakes.

However, a direct comparison between the Radon transform and the CNN prediction is challenging for several reasons. Technically, these local peaks must be identified manually, which prevents automatic operations on large datasets. Furthermore, the local peaks in the Radon space shown in figure 7 are less distinct than the clusters identified from the Radon transform of satellite data used by Zilman et al. (2004) (an example where the local peaks cannot be identified from the training data is shown in the Supplementary Material). This is likely because the relatively high spatial resolution and small domain size of the training data (compared with satellite data) reduce the signal to noise ratio of the asymptotic line patterns.

4.2 Result interpretation

One caveat of pure data-driven machine learning models is that the training process is a 'black box', which poses challenges to the interpretation of the result. To address this issue, we resort to the Shapley value, a concept originally developed for quantifying the contribution of each player in game theory (Shapley, 1953) for interpreting the prediction capability of neural network. The classical Shapley value is defined as

$$\phi_i = \sum_{S \subseteq F \setminus \{i\}} \frac{|S|!(|F| - |S| - 1)!}{|F|!} \left[f_{S \cup \{i\}} \left(x_{S \cup \{i\}} \right) - f_S \left(x_S \right) \right], \qquad (4.2)$$

where $f(x)$ is the model to be evaluated, with x being the input vector, F the (full) set of all features and ϕ_i measures the contribution of the ith component of x. Here, the summation loops over all subsets S of F when the ith component is excluded in the prediction.

Directly computing (11) is computationally too demanding, because the number of subsets $|S|$ grows fast with the dimension of the input data. Therefore, we compute the SHAP (SHapley Additive exPlanation) values that are the Shapley values of a conditional expectation function of the original model (Lundberg and Lee, 2017). The results for three example inputs are shown in figure 8. The spatial distributions of large SHAP value show a strong correlation with both the diverging and transverse waves in the Kelvin wakes, suggesting that the CNN prediction is based on the wave kinematics identified. As a comparison, the asymptotic wake angle (see figure 2) only identifies the local maximum of surface elevation that is heuristically determined.

4.3 Impact of nonlinearity

To evaluate the impact of nonlinearity on the prediction performance of CNN, we perform nonlinear simulations of Kelvin wakes generated by an elliptical pressure. The parameters of the surface disturbance are $U/\sqrt{gL} = 0.6$, $R/L = 5$ and $W = 0.5$, belonging to the dataset T_e. Six simulations are performed with varying pressure amplitude such that the characteristic wave steepness ϵ varies between 2.5×10^{-3} (weakly nonlinear) and 0.29 (strongly nonlinear). To demonstrate the nonlinear effect on the wave profiles, we plot the surface elevation along the transverse (y) direction at three locations behind the geometric centre of the surface disturbance (figure 9a). As shown, the broadening in the wake angle with increased nonlinearity agrees well with the findings of Dommermuth and Yue (1988).

Using the same data augmentation for generating the training data, the raw data in these nonlinear simulations are transformed into a validation dataset, which is then fed into the pretrained CNN model for predicting the velocity and the length scale. In figure 9(d), the prediction accuracy $A(U)$ and $A(L)$ are plotted as function of the characteristic wave steepness ϵ, an indicator of nonlinearity. As ϵ increases, $A(U)$ is largely unchanged. Therefore, to train a neural network model for predicting the velocity of the disturbance, it is sufficient to generate Kelvin-wake patterns from a linear wave model. In contrast, $A(L)$ sees a significant decrease with increased nonlinearity. The sensitivity of $A(L)$ to nonlinearity suggests that the CNN model better captures the wave dynamics compared with the velocity.
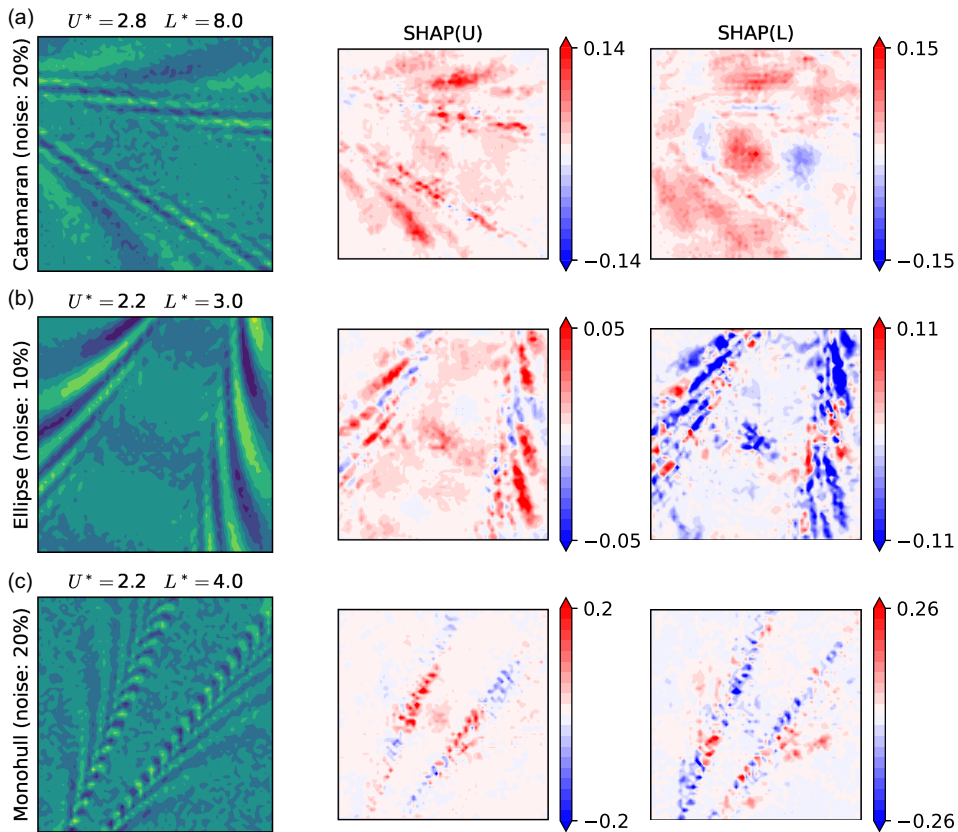
Figure 8. *The SHAP values computed for selected examples of pressure disturbance of type: (a) catamaran, (b) ellipse, (c) monohull. Here, the left, middle and right columns correspond to the input data (i.e. the normalised surface elevation), SHAP value corresponding to the prediction of U and the prediction of L, respectively.*

5. Conclusions

We have presented a CNN-based framework for predicting ship characteristics. By leveraging a phase-resolved wave model, we have simulated Kelvin wakes produced by surface disturbances of varying types. It is found that the CNN model trained from the wave data shows an excellent performance in predicting the disturbance speed and a satisfactory performance when predicting the disturbance length scale. We have revealed two important features of the prediction performance of CNN in inferring the disturbance properties that were rarely explored in pure data-driven based studies. First, it is found that the SHAP values are strongly correlated with the transverse and diverging wave patterns, which not only substantiates the capability of CNN as a reliable prediction tool but also paves the way for building a further connection between CNN and Kelvin-wake dynamics in future studies. Additionally, we have, for the first time, demonstrated that the nonlinearity impact on the prediction accuracy of the pretrained CNN model varies significantly depending on the prediction quantity.

The present study has demonstrated several advantages of supervised machine learning based on CNNs over unsupervised algorithms. For unsupervised algorithms, such as the Radon transform, an empirical relation is required to quantify the disturbance velocity and length scale from the features extracted from the raw data (see discussions by Zilman *et al.,* 2004). In contrast, this step is unnecessary for CNNs, as the labelled training data are generated from physics-based simulations. In other words, the CNN model itself serves as a reduced-order model of the underlying wave physics. Additionally, given
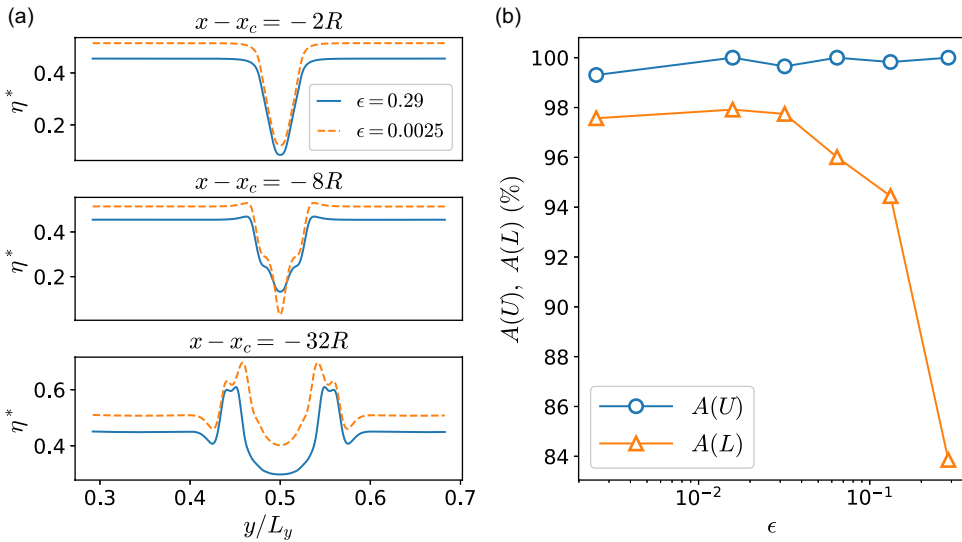
Figure 9. *(a) Normalised surface elevation along various transverse locations in the weakly ($\epsilon = 0.0025$) and strongly ($\epsilon = 0.29$) nonlinear cases and (b) prediction accuracy as a function of the characteristic wave steepness.*

the universal approximation capability of deep neural networks (Hornik *et al.*, 1989), the CNN-based prediction framework can be readily adapted to predict other quantities, such as the type of disturbance. From an efficiency perspective, while producing the training data and training a CNN model are computationally expensive, making predictions using a trained ResNet-18 model can be done in real time on modern CPUs and GPUs.

We remark that the present study also sees several promising extensions in future studies. For instance, the performance of the CNN can be further examined against a physics-based data assimilation framework that leverages the HOS method to incorporate the surface wave dynamics (Wang and Pan, 2021; Wang *et al.*, 2022; Wu *et al.*, 2022; Wu *et al.*, 2023). While we have only considered the Kelvin-wake part of ship wakes in this study, the same approach can be applied to non-Kelvin-wake parts, such as breaking waves, bubbly flows and viscous wakes (Reed and Milgram, 2002; Spedding, 2014) provided that the training data are generated by turbulent simulations based on the Navier–Stokes equations. Finally, the process for extending this framework to realistic remote sensing data is outlined. The training data (i.e. the synthetic normalised radar cross-section) can be generated by applying a transfer function to the surface elevation data (see review by Rizaev *et al.*, 2022). A CNN model can then be trained using the synthetic satellite data as input to predict the ship characteristics.

Ethical standards. The research meets all ethical guidelines, including adherence to the legal requirements of the study country.

References

Alam, M.-R. (2012). Broadband cloaking in stratified seas. *Physical Review Letters*, *108*(8), 084502.

Alam, M.-R., Liu, Y., & Yue, D. K. P. (2009). Bragg resonance of waves in a two-layer fluid propagating over bottom ripples. Part II. Numerical simulation. *Journal of Fluid Mechanics*, *624*, 225–253.

Benzaquen, M., Darmon, A., & Raphaël, E. (2014). Wake pattern and wave resistance for anisotropic moving disturbances. *Physics of Fluids*, *26*(9), 092106.

Copeland, A. C., Ravichandran, G., & Trivedi, M. M. (1995). Localized Radon transform-based detection of ship wakes in SAR images. *IEEE Transactions on Geoscience and Remote Sensing*, *33*(1), 35–45.

Darmon, A., Benzaquen, M., & Raphaël, E. (2014). Kelvin wake pattern at large Froude numbers. *Journal of Fluid Mechanics*, *738*, R3.

Dommermuth, D. G., & Yue, D. K. P. (1987). A high-order spectral method for the study of nonlinear gravity waves. *Journal of Fluid Mechanics*, *184*, 267–288.

Dommermuth, D. G., & Yue, D. K. P. (1988). The non-linear three dimensional waves generated by a moving surface disturbance. In Proceedings of the 17th Symposium on Naval Hydrodynamics, Hague, Netherlands. Washington DC: National Academy Press, pp. 523–549.

He, K., Zhang, X., Ren, S., & Sun, J. (2016). Deep residual learning for image recognition. In 2016 IEEE Conference on Computer Vision and Pattern Recognition (CVPR)Las Vegas, NV, USA: IEEE, pp. 770–778.

Hornik, K., Stinchcombe, M., & White, H. (1989). Multilayer feedforward networks are universal approximators. *Neural Networks*, *2*(5), 359–366.

Kang, K.-M., & Kim, D.-j. (2019). Ship velocity estimation from ship wakes detected using convolutional neural networks. *IEEE Journal of Selected Topics in Applied Earth Observations and Remote Sensing*, *12*(11), 4379–4388.

Kingma, D. P., & Ba, J. (2015, May 7–9). Adam: A method for stochastic optimization. In Y., Bengio & Y., LeCun(eds.), 3rd International Conference on Learning Representations, ICLR, 2015, San Diego, CA, USA, *Conference Track Proceedings*.

Kundu, P. K., Cohen, I. M., & Dowling, D. (2016). *Fluid mechanics*. Elsevier.

Lecun, Y., Bottou, L., Bengio, Y., & Haffner, P. (1998). Gradient-based learning applied to document recognition. *Proceedings of the IEEE*, *86*(11), 2278–2324.

Lundberg, S. M., & Lee, S.-I. (2017). A unified approach to interpreting model predictions. In Proceedings of the 31st International Conference on Neural Information Processing Systems, NIPS'17, Red Hook, NY, USA: Curran Associates Inc, pp. 4768–4777.

Mei, C. C., Stiassnie, M., & Yue, D. K. P. (2005). *Theory and applications of ocean surface waves*. Singapore; Hackensack, NJ: World Scientific.

Miao, S., & Liu, Y. (2015). Wave pattern in the wake of an arbitrary moving surface pressure disturbance. *Physics of Fluids*, *27*(12), 122102.

Mohaghegh, F., Murthy, J., & Alam, M.-R. (2021). Rapid phase-resolved prediction of nonlinear dispersive waves using machine learning. *Applied Ocean Research*, *117*, 102920.

Pan, Y. (2020). High-order spectral method for the simulation of capillary waves with complete order consistency. *Journal of Computational Physics*, *408*, 109299.

Pethiyagoda, R., Moroney, T. J., Lustri, C. J., & McCue, S. W. (2021). Kelvin wake pattern at small Froude numbers. *Journal of Fluid Mechanics*, *915*, A126.

Rabaud, M., & Moisy, F. (2013). Ship wakes: Kelvin or Mach angle? *Physical Review Letters*, *110*(21), 214503.

Radon, J. (1986). On the determination of functions from their integral values along certain manifolds. *IEEE Transactions on Medical Imaging*, *5*(4), 170–176.

Reed, A. M., & Milgram, J. H. (2002). Ship wakes and their radar images. *Annual Review of Fluid Mechanics*, *34*(1), 469–502.

Rizaev, I. G., Karakuş, O., Hogan, S. J., & Achim, A. (2022). Modeling and SAR imaging of the sea surface: a review of the state-of-the-art with simulations. *ISPRS Journal of Photogrammetry and Remote Sensing*, *187*, 120–140.

Scarpa, G. M., Zaggia, L., Manfè, G., Lorenzetti, G., Parnell, K., Soomere, T., Rapaglia, J., & Molinaroli, E. (2019). The effects of ship wakes in the Venice Lagoon and implications for the sustainability of shipping in coastal waters. *Scientific Reports*, *9*(1), 19014.

Shapley, L. S. (1953). A value for *n*-person games. In H. W. Kuhn, & A. W. Tucker (Eds.), *Contributions to the theory of games (AM-28)*, vol. *II*, pp. 307–318. Princeton University Press. 17

Spedding, G. R. (2014). Wake signature detection. *Annual Review of Fluid Mechanics*, *46*(1), 273–302.

Thomson, W. (1887). On ship waves. *Proceedings of the Institution of Mechanical Engineers*, *38*(1), 409–434.

Wang, G., & Pan, Y. (2021). Phase-resolved ocean wave forecast with ensemble-based data assimilation. *Journal of Fluid Mechanics*, *918*, A19.

Wang, G., Zhang, J., Ma, Y., Zhang, Q., Li, Z., & Pan, Y. (2022). Phase-resolved ocean wave forecast with simultaneous current estimation through data assimilation. *Journal of Fluid Mechanics*, *949*, A31.

Wu, J., Hao, X., Li, T., & Shen, L. (2023). Adjoint-based high-order spectral method of wave simulation for coastal bathymetry reconstruction. *Journal of Fluid Mechanics*, *972*, A41.

Wu, J., Hao, X., & Shen, L. (2022). An improved adjoint-based ocean wave reconstruction and prediction method. *Flow*, 2, E2.

Xiao, W., Liu, Y., Wu, G., & Yue, D. K. P. (2013). Rogue wave occurrence and dynamics by direct simulations of nonlinear wave-field evolution. *Journal of Fluid Mechanics*, *720*, 357–392.

Xue, F., Jin, W., Qiu, S., & Yang, J. (2022). Rethinking automatic ship wake detection: State-of-the-art CNN-based wake detection via optical images. *IEEE Transactions on Geoscience and Remote Sensing*, *60*, 1–22.

Zakharov, V. E. (1968). Stability of periodic waves of finite amplitude on the surface of a deep fluid. *Journal of Applied Mechanics and Technical Physics*, *9*(2), 190–194.

Zhang, Y., & Jiang, L. (2020). A novel data-driven scheme for the ship wake identification on the 2-D dynamic sea surface. *IEEE Access*, *8*, 69593–69600.

Zilman, G., Zapolski, A., & Marom, M. (2004). The speed and beam of a ship from its wake's SAR images. *IEEE Transactions on Geoscience and Remote Sensing*, *42*(10), 2335–2343.